Bautista, A., Pomares, J.C., González, M.N., Velasco, F. (2019). Influence of the microstructure of TMT reinforcing bars on their corrosion behavior in concrete with chlorides. *Construction and Building Materials*, v. 229, 116899, pp.: 1-11.

DOI: https://doi.org/10.1016/j.conbuildmat.2019.116899

Highlights:

- Corrosion studies of TMT bars in simulated pore solutions and in concrete slabs.
- The outer martensite acts as anode and the core as cathode when both parts of the bar are coupled.
- The core material does not meaningfully increases the corrosion rate of the outer martensite.
- The usual depth of the pits is related to the microstructure of the TMT bars.
- Once the pits reach the martensite-core interlayer, they tend to progress by mouth widening.

Graphical abstract

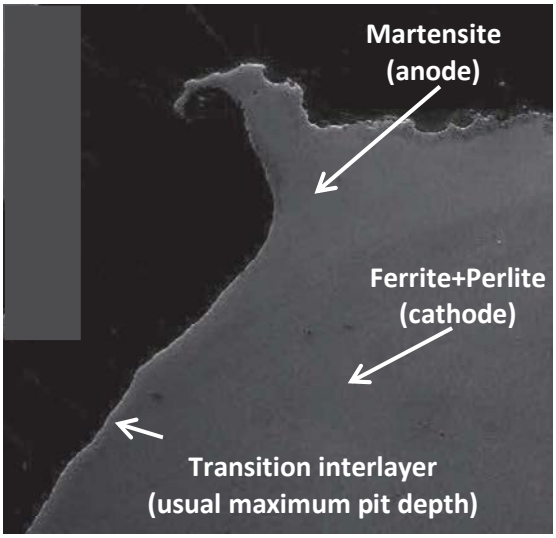

Influence of the microstructure of TMT reinforcing bars on their corrosion behavior in concrete with chlorides

A. Bautista[a1], J.C. Pomares[b], M.N. González[c], F. Velasco[a]

[a] University Carlos III of Madrid. Material Science and Engineering Department-IAAB. Avda. Universidad 30. 28911 Leganés, Madrid, Spain

[b] University of Alicante. Civil Engineering Department. Carretera San Vicente del Raspeig s/n, 03690 San Vicente del Raspeig, Alicante, Spain

[c] Universidad Politécnica de Madrid. Escuela Técnica Superior de Edificación. Avda. Juan de Herrera 6. 28040 Madrid, Spain

Abstract

Thermomechanically treated (TMT) carbon steel bars, often known as TempCore™ bars, are commonly used as reinforcements in concrete structures. TMT causes the formation of a martensite case in the outer surface of the bars, increasing their hardness, while the remaining ferritic-perlitic core maintains the typical ductility of hot rolled bars. In this work, the effect of this TMT induced microstructure on the development of pitting attacks in chloride media has been analyzed in depth. Electrochemical impedance spectroscopy (EIS) measurements and polarization curves have been carried out in simulated pore solutions to understand the effect of the presence of different phases in the microstructure and to quantify the strength of the galvanic couple that the outer martensite can form with the inner core. Moreover, accelerated corrosion tests in chloride contaminated concrete slabs have been performed. Bars from six different slabs where corrosive attack has been forced for different times have been studied. The shape of the main pits in the bars corroded in concrete has been analyzed through optoelectronic microscopy and the results obtained prove that the depth of the attack is related to the microstructure of the TMT bars.

Keywords: corrosion; pitting; chloride; concrete; thermomechanical treatment; carbon steel; galvanic coupling.

[1] Corresponding author. E-mail address: mbautist@ing.uc3m.es

1. Introduction

Reinforcing steel bars are usually embedded in concrete to increase the tensile properties of this material. They tend to corrode in chloride contaminated environments, being this problem one of the main causes of in-service failure of the structure. The initiation period of corrosion is the time needed for these depassivant ions to diffuse through the concrete cover and reach a critical concentration on the surface of the rebar high enough to cause the onset of the corrosion. This period usually implies the most significant part of the service life of the structures in marine atmospheres and its length depends on the porosity, thickness and other characteristics of the concrete cover [1,2]. Moreover, the microstructure and chemical composition of the bars can also affect the critical chloride content and other aspects very relevant for in-service performance of the structure, as the location and morphology of the attack.

Cold rolled carbon steel bars can offer higher mechanical strengths than traditional hot rolled bars [3,4], but the former are less ductile than the latter. Moreover, the stresses in the microstructure of cold rolled bars can make them more prone to corrosion, as it has been determined by mass loss tests carried out in solutions [5], and they present worse after-fire mechanical properties [3,4]. To increase the mechanical properties of hot rolled carbon steel bars, the addition of microalloying elements as well as thermomechanical treatment (TMT), can be used [6]. The addition of carbon in amounts ranging between 0.3 and 0.5% hardens the steel, but its bendability and weldability decrease [7], and, when considered that range of carbon contents the carbon equivalent can easily overpass the limit of 0.5% fixed in standards as EN10080 [8].

TMT bars, often known as TempCore^{TM} bars, are manufactured by passing the red heated steel -just after the rolling process- through a chamber with a control water flow that quenches the outer surface of the bars, while their core remains hot as austenite [9]. A martensite case is formed in the outer part of the bar. Then, in the core, the austenite is transformed into ferrite and perlite through a slow cooling, while the heat dissipated from the center of the bar to the surface causes the self-tempering of the previously formed martensite [10]. The martensitic case formed in the outer surface of the bars increases their hardness [11], while the remaining ferritic-perlitic core maintains the typical ductility of hot rolled bars. The final strength of the TMT rebars depends on the thickness of the outer tempered martensitic case as well as on the distribution of other phases inside the core of bar [12]. Nowadays, the use of TMT

carbon steel bars has become common for reinforcement of concrete structures in Europe.

There are studies published on the influence of the microstructure of TMT carbon steel bars on the fracture mode and ultimate tensile strength of the bars [9]. Moreover, TMT bars have shown better results in tensile and impact tests than direct air-cooled microalloyed hot rolled bars [13]. The influence of high-temperature exposure on the mechanical properties of the TMT bar is a point that has also been studied [3,14], with their results being worse than those shown for traditional hot-rolled carbon steel bars [3]. The fatigue performance of TMT bars has also been investigated [15].

The corrosion performance of the steel reinforcements is another key factor for the in-service performance of the structures. The alkaline solution inside the concrete pore should be able to guarantee the chemical durability of the steel. However, factors such as the presence of chlorides [16] or the decrease of the pore solution pH caused by carbonation [17] often provoke the active corrosion of the reinforcing steel bars. Microalloying elements that are able to improve moderately the corrosion resistance in saline solutions of the steel bars can also be added to TMT bars [18].

There is a corrosion study carried out with TMT bars where weight losses after sea water and fresh water immersions were measured [5]. The results obtained in this research suggest that the corrosion resistance of TMT bars could be higher than that of conventional hot rolled reinforcing bars. Another corrosion study with TMT bars also reports weight losses in NaCl solutions [6]. Recent preliminary results on the effect of the galvanic coupling between TMT and conventional reinforcement steels on their corrosion performance in simulated pore solutions have also been published [19].

Moreover, it has been conclusively proved that the morphology of the pits is a key factor influencing the tensile [20-22] and the fatigue [23,24] behaviors of the reinforcing bars, and so, it determines the likelihood of dangerous pathologies or in-service failures for the structures. The relationship between the microstructure of the reinforcing bars and their pit morphology has been analyzed in depth for stainless steel corrugated bars in simulated pore solutions, demonstrating that the size and distribution of the pits is related to different stresses and grain sizes caused by the forming process [25]. There are also previous studies about corrosion development of carbon steel in concrete [26,27], but they have not considered the possible influence of the specific microstructure that appears in the bars after TMT.

The frequent use of TMT bars and the clear interest of corrosion performance evidence the need for obtaining more complete information about how the phases present in their microstructure can influence the development of the attack in the bars. In this work, the influence of the microstructure originated by the TMT on the corrosion behavior of reinforcing bars is analyzed in solution tests, using different electrochemical techniques. The relative corrosion resistance of the phases present in the bars, their interaction and the resulting impact on the corrosion mechanism are analyzed. There are several factors implied in the onset and development of the corrosion of steel in concrete that are impossible to replicate in solution tests [28]. Hence, bars are heavily corroded in concrete slabs for different times, and a morphological analysis of the shape of the main pits detected is carried out to verify the results obtained in solution about the influence of the microstructure in the development of the pits.

2. Experimental

Carbon steel TMT bars type B-500-SD (EN 10080 [8] and UNE 36065 [29]) with 12-mm of diameter were used for this study. The chemical composition of the bars was determined from X-ray fluorescence and combustion infrared detection of C and S, which can be seen in **Table 1**. The alloying content of these bars makes their carbon equivalent 0.45%–calculated using the expression previously given by other authors [9,30]-. The Cu content detected (higher than 0.2%) is enough to assume a slight corrosion inhibition effect, based on previous published studies [18].

The microstructure of cross-sectional views of the bars was observed in metalographically prepared samples etched using Nital (5% HNO_3 in ethanol). Microhardness Vickers HV0,1 (100 gf) profiles were carried out in the cross-sections of the bars. Measurements started about 50 μm from the ribbed surface of the bar and they were performed each 100 μm. For this study, a Zwick Roell Indentec machine was used. Localized hardness measurements complete the information about the microstructure of the bars and can inform about possible residual stresses. These are aspects that can affect the corrosion performance of different areas of the bar.

For the electrochemical corrosion tests carried out in solution, two types of samples were used: a) samples from the corrugated surface of the TMT bars, labelled as “Ribbed surface”; and b) samples machined from TMT bars where the martensite case had been fully removed, labelled as “Core”. The “Core” cylinders had a diameter of 9 mm. Both types of samples were cut into 3-cm long cylinders, as can be seen in

Figure 1. The surface of the "Ribbed surface" samples was mechanically cleaned before the tests to erase any oxide formed due to the atmospheric exposure of the as-received bars, using a Dremel Multipro tool. The mill-scale of the surface of the "Ribbed bars" was kept after this soft cleaning process. Before being immersed in the testing solution, a copper wire was glued to one of the cross-sections of each sample using silver paint. Then, both cross-sections were covered with epoxy coating to avoid their interference in the measurement results.

The testing solution used to simulate that contained inside the pores of a chloride contaminated concrete [19] was 0.1 M NaOH, 0.3 M KOH and 0.15 M NaCl. The pH of this solution was 13.2. Four different samples have been tested for each steel in each type of electrochemical measurement.

The galvanic current flowing between "Ribbed surface" and "Core" samples in this solution was measured using a 263A Potentiostat/Galvanostat from PAR. For this measurement, the ratio of the surfaces Ribbed surface/Core was 1.66.

Polarization curves and electrochemical impedance spectroscopy (EIS) measurements were carried out for the "Ribbed surface" and "Core" samples in the previously detailed solution. Moreover, these electrochemical tests were also performed in short-circuited samples of "Core" and "Ribbed surface" connected through a wire. This third type of samples will be called "Galvanic couple" hereafter. Those techniques have been used in the field for decades and allow to obtain a very sensitive, reliable information about the kinetics and mechanism of electrochemical processes.

A three-electrode cell was used in these studies. A saturated calomel electrode (SCE) was used as reference electrode, and an AISI 316 stainless steel coiled wire as counter electrode. The open circuit potential (OCP) of all the samples was allowed to stabilize for 45 min in the testing solution. Then, the non-destructive EIS tests were carried out at OCP and, finally, the polarization curves were performed. EIS measurements were carried out from 100 kHz to 10 mHz applying a sinusoidal perturbation of 10 mV_{rms}. The polarization curves started at -200 mV from the previously determined OCP, and the potential was increased towards more anodic values at a rate of 0.5 mV/s. The Tafel slopes in the polarization curves were calculated from ±70 mV vs. E_{corr} (corrosion potential) to higher overpotentials. Those electrochemical measurements were done using a Solartron Analytical Potentiostat/Galvanostat from Ametek. More information about the background of electrochemical tests can be found elsewhere [31,32]

With the aim of checking the results of electrochemical techniques, TMT steel reinforcements were extensively corroded in concrete. 50-cm long bars of the same ribbed TMT steel were used to perform corrosion studies in concrete slabs with 500 x 265 x 100 mm dimensions. Six slabs were manufactured, embedding in each one 10 steel bars with a 37-mm distance between each bar. The cement used was CEM II/B-L 32.5 N, and the water/cement ratio was 0.45. The cement/sand/coarse aggregate ratios used were 1/2/3. A 3.3% $CaCl_2$ regarding the weight of cement was also added to the mixture, as other authors have previously done to increase the chloride content in mortars and concretes [33]. The regions of the bars close to the concrete-air interface were protected with an isolating tape, with an approximately 25-cm length of the bar exposed to corrosion inside the concrete. In **Figure 2**, an image of one of the reinforced concrete slabs manufactured for performing the present research can be seen.

After casting, the 6 slabs were cured at high relative humidity and room temperature for 28 days, and then the corrosion of the rebar was accelerated by impressed currents. Bars embedded in the different slabs were submitted to accelerated corrosion for 6 different times (70, 120, 160, 220, 280 and 350 days) to achieve different levels of attack. The current density in each of the bars was initially 80 $\mu A/cm^2$. This corrosion density was about one order of magnitude higher than the corrosion rates determined for in-service structures exposed to chloride environments and high relative humidity [34]. The method was already used and described in previous studies [35,36]. As the slabs cracked extensively, especially for the longer tests, the used power sources were unable to keep this current densities. For the slabs corroded more than 160 days, the supplied currents decreases down to about 10 $\mu A/cm^2$. After the accelerated corrosion tests in concrete, the slabs were broken, and the oxides generated on the surface of the reinforcing bars were cleaned using a HCl solution inhibited with urotropine. The main pits in each bar were identified and their morphology was characterized by optoelectronic microscopy, with the measurements done using an Olympus DSX500. Optoelectronic microscopy is a technique that has recently been used to characterize the morphology of pits and evaluate its dangerousness in other materials [37]. Moreover, scanning electron microscopy (SEM) was used to check the relationship between pit depth and microstructure.

3. Results and discussion

3.1. Electrochemical characterization in solution

In **Figure 3,** optical microscopy images corresponding to etched cross-sections of the TMT bars can be observed. In **Figure 3a,** the outer case -with a clearly darker microstructure after the attack- can be easily distinguished from the inner region of the corrugated bar. In **Figure 3b,** obtained at higher magnifications, it can be checked that the inner core of the bar is formed by ferrite and perlite, as corresponds to a steel with a C content as that shown in **Table 1** and which has been cooled from the austenitic state at a slow enough cooling rate. **Figure 3c** shows the transition region between the core and the outer case. The thickness of the transition interlayer seems to be much reduced, which suggests that the quenching procedure to form the outer layer has been carried out adequately [9]. The presence of bainite in this interlayer has been often mentioned in previous literature [13], but, for the studied bars, it is difficult to assure with reliability the presence of this phase. Moreover, other authors have neither found noticeable bainite in the microstructure of the bars nor have predicted its presence by the modeling of the TMT process [11]. The microstructure observed in the transition zone is compatible with ferritic and perlitic phases, which close to the martensite case would become finer -with a smaller grain size- than in the bulk of the bar (**Figure 3b**). In **Figure 3d**, the typical microstructure of martensite, obtained by the quenching and tempering of the surface during bar manufacture, can be observed.

There exists a clear relationship between microstructure, stresses and micromechanical properties. As the corrosion behavior of the bars can be very dependent on microstructure and stresses, a micromechanical study has been carried out. Some representative microhardness profiles obtained measuring from the surface of the bars towards regions where the micromechanical properties become stable can be seen in **Figure 4.** These results show a plateau with the highest hardness for regions close to the surface, proving the improvement in this property caused by the formation of martensite (**Figure 3d**). The thickness of this high hardness region depends on the exposure time to the water cooling during the martensite formation and on the cooling-water flow rate [11]. The length of the highest hardness plateau slightly oscillates (**Figure 4**). This result is coherent with the slight dispersion in the thickness of the outer martensite case observed in different sections of the bars and that can be guessed in images as that shown in **Figure 3a.** This lack of uniformity for the outer case could be related to the dispersion in the prior austenite grain sizes in the red heated steel during the bar processing [11]. Moreover, if the microhardness profiles start from a rib of the surface, the highest hardness plateau is defined at slightly higher values, probably because the faster cooling rate of this particular region causes the

formation of a finer grain martensite. The decrease in hardness after the plateau is very steep, which corresponds to the observations in **Figure 3c**.

There is also another plateau for the lowest measured hardness (**Figure 4**). The microhardness values can be considered completely stable from a surface distance higher than about 2.2 mm, if the profiles start from a point between ribs. Obviously, this stabilization distance is much higher if the measurement starts in a rib. Between this plateau of complete stabilization and the decrease in hardness corresponding to the transition zone, a region of hardness slightly higher than that of the plateau can be observed. This region with slightly higher hardness can be identified with finer perlite and ferrite than in the bulk material observed close to the martensite (**Figure 3**).

In chloride-containing solutions that, because of their pH, simulate those contained inside the concrete pores, there is a galvanic current density flowing between samples from the “Ribbed surface” and from the “Core” of the bars -as those shown in **Figure 1-** when they are short-circuited. The sign of the measured current always shows that the martensite from the surface of the ribbed bars acts as anode against the material in the core. Time records with oscillations and small transitories, as those shown in **Figure 5,** can be seen in this kind of experiments. To calculate the galvanic current density (i_{galv}), the surface of the anodic samples -that is to say, the area of the “Ribbed surface” samples- has been used. The mean values of i_{galv} determined from the different current distributions registered in the different experiments performed always ranged between 0.7 and 1.0 μA/cm^2. These results are coherent with the preferential corrosion of the martensite case of TMT rebars in chloride contaminated concrete reported in other works [35,36].

Polarization curves have been performed in simulated pore solution to obtain information about the relative corrosion rate of the different microstructures and how their short-circuiting can affect it. Moreover, a careful analysis of these curves can also give relevant information about the process determining the corrosion kinetics. Examples of the polarization curves obtained for “Ribbed surface” and “Core” samples can be seen in **Figure 6**. Moreover, an example of one of the curves obtained for “Galvanic couple” samples has also been included in the figure. All the curves are quite similar, and they can be considered typical for systems that corrode actively at moderate rates.

During the anodic polarization, the Tafel behavior (that is to say, the charge transfer control of the process) is found in the narrow range where a linear relationship among the potential and logarithm of the anodic current density is linear. For the studied systems, this occurs up to overpotentials of 120 mV or somewhat higher. At higher anodic overpotentials, the current almost slows down and its increase diverts from the Tafel behavior. This indicates the influence of another phenomenon different from the charge transfer in the anodic semireaction. The cathodic branches of the curves always shown a typical Tafel behavior that can be seen from potentials about 25 mV higher than the onset of the curves to about 70 mV vs. E_{corr} .

In **Figure 7**, the most relevant data that can be calculated from curves as those shown in **Figure 6** are plotted. The average values as well as the standard deviations of the experimental data obtained have been plotted. In **Figure 7a**, it can be seen that the E_{corr} determined for the different types of samples are typical of active steel following the probabilistic criterion proposed by the ASTM C876 standard [38]. For the solution used in the present study, the traditional $[Cl^-]/[OH^-]$ ratio employed to calculate the critical chloride and the depassivation of the steel has a value of 0.375. Previous published studies show a huge dispersion in this value, depending on the testing conditions and the method used to detect the depassivation [39]. In tests carried out in simulated pore solution using electrochemical techniques, a value of 0.35 has been determined as critical [40], so the testing solution used in the present research is somewhat above it. The more innovative $[Cl]/[OH^-]^3$ ratio with a critical value fixed at 1.25 has recently been proposed as more reliable [41]. This value has been determined in chloride solutions with different NaOH concentrations and electrochemical techniques. The simulated pore solution used in the present research has a $[Cl]/[OH^-]^3$ ratio of 2.3, so it is logical that the bars corrode actively. There is some dispersion for measured E_{corr} values for the same type of samples. Bearing in mind the overlapping of the error bars, it could be concluded that the E_{corr} of the three studied types of samples are similar from a statistical point of view.

The corrosion current densities (i_{corr}) are also very similar for the three types of samples (**Figure 7a**). All the measured i_{corr} are about one order of magnitude higher than 0.1 $\mu A/cm^2$, which is usually assumed to be a limit value for determining the onset of corrosion of carbon steel reinforcements [42]. The average value for the “Ribbed surface” is higher than for the “Core” (**Figure 7a**).

The most relevant information that can be drawn from the obtained polarization curves are the Tafel slopes. In **Figure 7b**, it can be seen that, for the three systems,

the anodic Tafel slopes (b_a) are always higher than the cathodic Tafel slopes (b_c). This fact means that the anodic process is the most hindered, and the i_{corr} is more controlled by anodic semireaction than by the cathodic one. At any rate, as the difference between b_a and b_c is not huge, a mixed control of the corrosion rate must be assumed, with a lower influence of the cathodic process. b_a is clearly higher for the "Core" than for other samples. This indicates that the anodic process is less favored in the ferrite and perlite than in the martensite. The b_a values allow to explain the i_{galv} observed (**Figure 5**) and the preferential corrosion of the martensite. On the other hand, b_c values are quite similar for all the studied systems, which implies that the oxygen reduction, that is the cathodic process in this medium, is not clearly easier on the microstructure of one surface than on the other. So, the cathodic reaction is not more favored on the ferrite-perlite than on the martensite. The i_{galv} observed in experiments such as that in **Figure 5** can only be justified by the higher trend of the martensite to locate the anodic reaction, while the cathodic process is not preferentially located neither on the outer martensite nor in "Core" material.

Hence, a galvanic couple is formed between martensite and ferrite, but its performance does not coincide with that of the most well-known galvanic couples, which are formed by metals with very different E_{corr}. In the case under study, the anodic process is mainly located in the martensite, but the cathodic process is not specially favored on any of the surfaces (as their b_c are very similar). For this reason, it is necessary to use only the surface of the martensite in the "Galvanic couple" samples to obtain reliable corrosion rates for the electrochemical tests. If the i_{corr} for the "Galvanic couple" in **Figure 7a** is re-calculated using only the surface of the martensite instead of the surface of both short-circuited samples, the average i_{corr} value increases up to a value similar to that of the "Ribbed surface".

On the other hand, the highest E_{corr} observed for the "Galvanic couple" must correspond to an increase in the cathodic area in these samples. The ferrite-perlite acts preferentially as a cathode, while the martensite also keeps cathodic activity besides locating preferentially the anodes. A higher cathodic area shifts the cathodic process to higher current intensities, and then the current balance between the anodic and the cathodic semireactions appears at higher potentials (higher E_{corr}).

These results informs than, when the pits go deep down to the core of the bar, a galvanic couple is formed between the martensite and the ferrite-perlite, being this last type of microstructure cathodically protected. So, once the corrosion has reached

the core of the bars, the attack should tend to develop preferentially through the martensite.

However, it could be assumed that the cathodic protection of the ferrite-perlite would increase the corrosion rate of the martensite, but, in fact, it does not seem feasible. Due to the steep anodic branch observed in the polarization curve for the "Ribbed samples" (**Figure 6**) and the small increase in the E_{corr} that takes place due to formation of "Galvanic couple", the foreseeable increase in the i_{corr} for the "Galvanic couple" is lower than the experimental dispersion determined for this parameter for the corroding systems studied. Thus, short-circuiting ferrite-perlite with martensite would not meaningfully increase the corrosion rate of the martensite in spite of the formed galvanic couple. In addition, it should be borne in mind that, when the short-circuiting takes place between the material of the core and that of the case because of a pit, the ratio anodic area/cathodic area is high, so the ability of the ferrite-perlite phase to increase the corrosion rate of the martensite will become quite reduced. Hence, the microstructure of TMT bars seems adequate to limit the development of very specially dangerous forms of corrosion. Anyway, it cannot be forgotten than inside the pits many chemical changes takes place (acid hydrolysis of the corrosion products, decrease on the oxygen amount, cells of ionic concentrations, etc.) that affect the eventual kinetic of the process [16], making the real development of the attack in structures a very complex process, dependent of many environmental factors.

With the aim of obtaining more information about the corrosion mechanism and the influence of the bar microstructure on it, EIS studies have been carried out. Examples of the EIS spectra obtained for the "Ribbed surface", "Core" and "Galvanic couple" samples are shown, as Bode and Nyquist diagrams, in **Figure 8**. To obtain an adequate simulation of spectra like these, a circuit equivalent as that proposed in **Figure 9** has been necessary. In this circuit, R_{sol} is the solution resistance between the counter electrode and the working electrode, and its influence can be seen at the highest frequencies. The electric behavior of the passive layer is simulated by the R_{pas} and CPE_{pas}. Identification of the influence of the passive layer with the time constant that appears in the spectra at medium-high frequencies is commonly found in previous literature [43,44]. R_{pas} simulates the electrical resistance of the passive layer and CPE_{pas} simulates its non-ideal capacitive behavior. The simulation fixes the CPE_{pas} impedance using two values: the C_{pas}, which is the capacitance determined for the passive layer and n_{pas} that is an empirical coefficient whose values can range between 0 and 1, being 1 when the behavior is ideal. The corrosion activity is identified with the phenomena which appear in the spectra at lower frequencies. The process is simulated

with elements that correspond to the charge transfer resistance inside the pits, R_{pit}, and the capacitive behavior of the double layer inside the pits, CPE_{pit}. The CPE_{pit} is a constant phase element whose electrical performance is simulated using C_{pit} and n_{pit}. Moreover, to obtain a good simulation of the experimental data at the lowest frequencies, it is necessary to include a Warburg element related to the diffusion impedance through a finite thickness (W_s). The W_s impedance is simulated using three parameters, W_s-R, W_s-P and W_s-T. W_s-R can be identified with the resistance associated to the process, W_s-P is a coefficient whose value is 0.5 for ideal process, but can be lower for real processes, and W_s-T is the ratio between the square of the effective diffusion thickness and the diffusion coefficient of the specie. The equivalent circuit used to simulate the results is similar to the one already used to simulate the electrochemical behavior of corroding steel in concrete [43,45].

In steel embedded in chloride contaminated concrete, a diffusion impedance through a semi-infinite thickness is often identified at low frequencies. It has been assumed that this impedance reflects the influence that the diffusion impedance of oxygen through the concrete cover can have on the corrosion process. In solution tests such as those performed in this study, the access of oxygen to the rebar surface is higher and this hypothesis could be discarded, at least at moderate i_{corr} (**Figure 7a**). The diffusion of ions through the oxide layer has also been previously proposed as being responsible for the presence of diffusion impedance at the lowest-frequency part of the spectra in simulated pore solutions [41] and in concrete [44]. Hence, the W_s impedance could correspond to the diffusion through surface oxides. The polarization results (**Figure 6**) are coherent with this hypothesis, because of the region defined at anodic overvoltages and high current densities where the i hardly increases its values when E increases, and that can easily be identified with a current diffusion limit (related to W_s-R) and somewhat higher than i_{corr}.

Due to their higher order of magnitude, the parameters that have the most determining effect on the corrosion rate are R_{pit} and W_s-R, which have been highlighted in bold in **Table 2**. For all the studied systems, R_{pit} is higher than W_s-R, so the charge transfer resistance inside the pits can be identified as the rate determining step. However, the difference between R_{pit} and W_s-R is so small that it would be a sizeable mistake to omit the influence of the ions diffusion through the oxide. The global impedance of the process at low-frequencies (essentially R_{pit}+W_s-R) shows values for “Ribbed surface” that are half of those obtained for the “Core”, matching the trend obtained for the i_{corr} (**Figure 7a**).

3.2. Study of the bars corroded in concrete

The influence of the microstructure on the development of the pits has been checked carrying out accelerated tests in concrete. The long-term, aggressive tests carried out pretended to cause corrosive attacks that reach the ferrite-perlite core of the bars. In **Table 3**, information regarding the development of the corrosion process in the reinforcements and the size of the cracks can be seen. The supplied charge increases in a non-linear way with the length of the tests, as this parameter is affected by the onset and development of cracks in the concrete. Cracks suppose a clear obstacle for the current flow between the steel bars and the cathode. Thus, the current density that flows through extensively cracked slabs (at the end of the longest tests) is always lower than that initially applied. The corrosion rates have been calculated from the mass losses determined after the tests. It can also be seen that, though the mass losses of the bars increase with the length of the test, the corrosion rates decrease. This can be easily related to the decrease on the current that flows after concrete cracking.

The minimum values for current efficiencies (**Table 3**) have been calculated assuming that the Fe is always oxidized to FeO. The highest values calculated for efficiency range of each slab corresponds to the theoretical assumption that all the Fe is oxidized to Fe(III). The additional formation of compounds more oxidized than FeO, as Fe_2O_3 or Fe_3O_4, cannot be discarded, especially when the steels are exposed to the air through the cracks. Anyhow, the use of part of the current for other electrochemical reactions, as water evolution, can also be considered, and these phenomena would affect the efficiency too.

Macroscopic images of the corrosion that has taken place in the slabs, after the oxides have been removed, are shown in **Figure 10**. It can be seen that big pits tend to develop in the corrugated surface of the bars. The SEM images in **Figure 11,** corresponding to one of the pits, allow to verify that the attack tends to initially develop through the martensite, forming a slightly jagged surface on this phase due to the attack (**Figure 11a**). When the corrosion reaches the thin interlayer formed between the martensite and the ferritic and perlitic region, the deepening of the attack seems restrained and the bottom of the pit becomes smother (**Figure 11b**).

To perform a more exhaustive study regarding the pit morphology of TMT bars in chloride contaminated concrete, the depth and surface area of the main pits detected in corroded reinforcing TMT steel have been measured using optoelectronic microscopy. Images such as that shown in **Figure 12** are obtained for the main pits formed in the bars. The mass loss of each studied pit plotted in **Figures 13** and **14** has

been calculated from the volume of the pit given by its optoelectronic characterization and using the density of the steel. Numerous pits whose mass losses differ more than two orders of magnitude –in grams- have been considered for this study.

In **Figure 13**, it can be seen that the increase in volume of the pits is clearly associated to an increase in the area of the pits mouths. Pits whose areas vary more than two orders of magnitude –in mm^2- have been detected. The pits with the highest individual mass losses and with the highest mouth areas appear in bars embedded in the slabs that have been corroded for the longest times.

At any rate, the results in **Figure 14** prove that the pits associated to the lowest mass losses tend to have maximum depths lower than that of the martensitic case, confirming the observation carried out for images like that in **Figure 11a.**

The obtained results suggest that the attack initially takes place in the martensitic case and that, when the corrosion reaches the martensite-ferrite interlayer, the pits tend to continue their growth by mouth widening through the martensitic case. Only when the pits become very big, can this trend disappear, due to loss of galvanic effect that would cause the increase of the ohmic drop between preferential anode or cathodes. Obviously, if the ionic electrolyte disappears between the different microstructures by concrete cracking, the galvanic effect on the corrosion would also disappear.

In **Figure 14**, the relationship between the volume/mass loss of each characterized pit and its maximum depth is plotted. The pit depth is a parameter that, for the pits most easily detectable by visual inspection, varies slightly. All the obtained values from the pit depth differ in less than one order of magnitude, though the volume of the pits is quite different. Moreover, most of the determined maximum pit depths are between 1-2 mm. If it is born in mind that the software always takes into account the maximum height appearing in the image as a reference for calculating the depth of the pits, and that the height of ribs and nerves often influence this value, it is obvious that the calculated maximum pit depth matches the thickness where the typical microstructure of the core appears (**Figure 3**) and the lowest hardness plateau onsets (**Figure 4**). Thus, these data confirm observations as those in **Figure 11b**, which suggest that the attack tends to be stopped in the transition interlayer. The fact that sometimes values for the pit depth slightly higher than the typical values obtained for the martensitic case of the studied TMT steel have been obtained with this technique could suggest that, for the biggest pits, the cathodic protection that the martensite offers to the ferrite and perlite would disappear. This can be due to the ohmic drop that

should appear between the bottom of the pit and the outer surface for the biggest pits. Moreover, the progress of the pits could also be affected by the concrete cracking (**Table 3**) that, for the longest tests, may expose directly part of the reinforcing steel to the atmosphere

The results obtained in the laboratory, from solution tests where TMT bars corrode at moderate corrosion rate, match with those obtained from tests in concrete where TMT bars corrode at very high corrosion rate. However, the morphology of the pits in the accelerated tests in concrete can be affected by factors such as the high anodic polarizations under the attack has been developed. Hence, it would be interesting to check these results with an additional study of the pitting morphologies that can appear in TMT bars real structures in different in-service aggressive exposure.

4. Conclusions

The results obtained in this study reveal how the microstructure characteristic of TMT affects the development of the pits in concrete or simulated pore solutions with chlorides. The main conclusions that can be drawn the results obtained are:

- The i_{corr} of the martensite is slightly higher than that of the ferrite-perlite in solution tests and their E_{corr} are similar.
- The galvanic coupling between the martensite and the ferrite-perlite in solution tests proves that the martensite tends to act as anode and the ferrite-perlite as cathode.
- The anodic semireaction of the martensite is more hindered than the cathodic one in the testing solution, so a small increase in the cathodic surface that a pit reaching to the core would imply, does not cause a meaningful increase in the corrosion rate of the outer case.
- The EIS results obtained in solution inform that the charge transfer inside the pores is the most determining phenomenon for the corrosion rate, but there exists a mixed control. The influence of the diffusion impedance through the oxide layer should also be considered.
- Results obtained in concrete prove that the depth of the attack is determined by the microstructure of the TMT bars. Once the corrosion has reached the ferritic-

perlitic core, the attack tends to progress mainly by pit widening until the volume of the pit is very large and/or the concrete cover cracks.

Acknowledgments

The authors acknowledge the financial support of Interreg SUDOE, through KrEaTive Habitat project (grant Ref. SOE1/P1/E0307).

References

[1] Y. Wang, X. Gong, L. Wu Prediction model of chloride diffusion in concrete considering the coupling effects of coarse aggregate and steel reinforcement exposed to marine tidal environment. Constr. Build. Mater. 216 (2019) 40-57. https://doi.org/10.1016/j.conbuildmat.2019.04.221

[2] J. Liu, Y. Jia, J. Wang. Calculation of chloride ion diffusion in glass and polypropylene fiber-reinforced concrete. Contr. Build. Mater. 215 (2019) 875-885. https://doi.org/10.1016/j.conbuildmat.2019.04.246

[3] R. Felicetti, P. G. Gambarova, A. Meda. Residual behaviour of steel rebars and R/C sections after fire. Constr. Build. Mater. 23 (2009) 35-46. https://doi.org/10.10.16/j.conbuildmat.2009.06050

[4] A.Y. Elghazouli, K.A. Cashell, B.A. Izzuddin. Experimental evaluation of mechanical properties of steel reinforcement at elevated temperature. Fire Saf. J. 44 (2009) 909-919. https://doi.org/10.1016./j.firesaf.2009.05.004

[5] M.A. Islam. Corrrosion behaviour of high strength TMT steel bars for reinforcing cement concrete structures. Proc. Eng. 125 (2015) 623-630. https://doi.org/10.1016/j.proeng.2015.11.084.

[6] S.K. Nandi, N.K. Tewary, J.K. Saha, S.K. Ghosh. Microstructure, mechanical properties and corrosion performance of a few TMT rebars. Corr. Eng. Sci. Techn. 51 (2016) 476-488. https://doi.org/10.1080/1478422X.2016.11141744.

[7] S.K. Paul, P.K. Rana, D. Das, S. Chadra, S. Kundu. High and low cycle fatigue performance comparison between micro alloyed and TMT rebar. Constr. Build. Mater. 54 (2014) 170-179. https://doi.org/10.1016/j.conbuildmat.2013.12.061

[8] EN 10080:2005 standard, Steel for the reinforcement of concrete - Weldable reinforcing steel - General.

[9] I.R. Kabir, M.A. Islam. Hardened case properties and tensile behaviors of TMT steel bars. Am. J. Mech. Eng. 2 (2014) 8-4. https://doi.org/10.12691/ajme-2-1-2

[10] H. Khalifa, G.M. Megahed, R.M. Hamouda, M.A. Taha. Experimental investigation and simulation of structure and tensile properties of Tempcore treated rebar. J. Mater. Process. Techn. 230 (2016) 244-253. https://doi.org/10.1016/j.jmatprotec.2015.11.023

[11] K. Bandyopadhyay, J. Lee, J.-H. Shim, B. Hwang, M.-G. Lee. Modeling and experiment on microstructure evolutions and mechanical properties in grade 600 MPa reinforcing steel rebar subjected to TempCore process. Mater. Sci. Eng. A 745 (2019) 39-52. https://doi.org/10.1016/j.msea.2018.12.079

[12] M. Mukherjee, C. Dutta, A. Haldar. Prediction of hardness of the tempered martensitic rim of TMT rebars. Mater. Sci. Eng. A 543 (2012) 35-43. https://doi.org/10.1016/j.msea.2012.02.041

[13] A. Ghosh, M. Ghosh. Tensile and impact behavior of thermomechanically treated and micro-alloyed medium carbon steel bar. Contr. Build. Mater 192 (2018) 657-670. https://doi.org/10.1016/j.conbuildmat.2018.10098.

[14] F. Tariq, P. Bhargava. Residual mechanical behavior of (SD 500) hot rolled TMT reinforcing steel bars after elevated temperatures. Constr. Build. Mater. 190 (2018) 551-559. https://doi.org/10.1016/j.conbuildmat.2018.09.008

[15] B. Das, A. Bakkar, N. Khutia, D. Das. Low cycle fatigue performance evaluation of TMT rebar. Mater. Today: Proc. 4 (2A) (2017) 2554-2563. https://doi.org/10.1016/j.matpr.2017.02.109

[16] J.A. Gonzalez, E. Otero, S. Feliu, A. Bautista, E. Ramírez, P. Rodríguez, W. López. Some considerations on the effect of chloride ions on the corrosion of steel reinforcements embedded in concrete structures. Mag. Concrete Res. 50 (1998) 189-199. https://doi.org/10.1680/macr.1998.50.3.189

[17] M. Otieno, J. Ikotun, Y. Ballin. Experimental investigations on the influence of cover depth and concrete quality on time to cover cracking due to carbonation-induced corrosion of steel in RC structures in an urban, inland environment. Constr. Build. Mater. 198 (2019) 172-181. https://doi.org/10.1016/j.conbuildmat.2018.11.215

[18] B.K. Panigrahi, S. Srikanth, G. Sahoo. Effect of alloying elements on tensile properties, microstructure, and corrosion resistance of reinforcing bar steel. JMEPEG 18 (8) (2009) 1102-1108. https://doi.org/10.1007/s11665-008-9336-z

[19] H. Tobarti-Sarraf, A. Poursaee. Corrosion of coupled steels with different microstructures in concrete environment. Constr. Build. Mater. 167 (2018) 680-687. https://doi.org/10.1016/j.conbuldmater.2018.02.083.

[20] W. Zhu, R. François, C.S. Poon, J.-G. Dai. Influences of corrosion degree and corrosion morphology on the ductility of steel reinforcement. Constr. Build. Mater. 148 (2017) 297-306. https://doi.org/10.1016/j.conbuildmat.2017705.079

[21] C.A. Apostopoulos, S. Demis, V.G. Papadakis. Chloride-induced corrosion of steel reinforcement- Mechanical performance and pit depth analysis. Constr. Build. Mater. 38 (2013) 139-146. https://doi.org/10.1016/ conbuild mat.2012.07. 087

[22] A. Castel, R. François, G. Arliguie. Mechanical behaviour of corroded reinforced concrete beams – Part 2: Bond and notch effects. Mater. Struct. 33 (2000) 545-551. https://doi.org/10.1007/BF02480534

[23] Y. Ma, W. Qianj, Z. Guo, G. Wang, L. Wang, J. Zhang. Static and fatigue behaviour investigation of artificial notched steel reinforcement. Materials 10 (2017) 532. https://doi.org/10.3390/ma10050532

[24] I. Fernández, J.M. Bairán, A.R. Martí. Corrosion effects on the mechanical properties of reinforcing steel bars. Fatigue and σ-ε behaviour. Constr. Build. Mater. 101 (2015) 772-783. https://doi.org/10.10016/j.conbuildmat.2015.10.139

[25] E.C. Paredes, A. Bautista, S.M. Alvarez, F. Velasco. Influence of the forming process of corrugated stainless steel on their corrosion behaviour in simulated pore solutions. Corros. Sci. 58 (2012) 52-61. https://doi.org/10.1016/j.corsci.2012.01.010

[26] W. Zhu, R. François. Y. Liu. Propagation of corrosion and corrosion patterns of bars embedded in RC beams stored in chloride environment for various periods. Constr. Build. Mater. 145 (2017) 147-156. https://doi.org/10.1016/j.conbuildmat.2017.03.210

[27] Z. Zhao, L. Fu. The probability distribution of pitting for accelerated corrosion reinforcement. Case Studies Contr. Mater. *(in press).* https://doi.org/10.1016/cscm.2018.e00193

[28] A. Bautista, E.C. Paredes, F. Velasco, S.M. Alvarez. Corrugated stainless steels embedded in mortar for 9 years: Corrosion results of non-carbonated, chloride-contaminated samples. Constr. Build. Mater. 93 (2015) 350-359. Doi: 10.1016/j.conbuildmat.2015.04.060

[29] UNE 36065:2011, Barras corrugadas de acero soldable con características especiales de ductilidad para armaduras de hormigón armado.

[30] R. Datta, R. Veeraraghavan, K.L. Rohira. Weldability characteristics of torr and corrosion-resistant TMT bars using SMAW process. Materi. Eng. Perform. 11 (2002) 369-375. https://doi.org/10.1361/105994902770343881

[31] A.J. Bard, L.R. Faulkner, Electrochemical methods: Fundamentals and applications, John Wiley and Sons, New York, 1980.

[32] J.R. Scully, Electrochemical tests, in: R. Baboian (Ed.), Corrosion Tests and Standards: Application and Interpretation, 2nd edition, ASTM, West Conshohocken, PA (USA), 2005, pp. 107-130.

[33] J.A. Gonzalez, J.M. Miranda, S. Feliu. Considerations on reproducibility of potential and corrosion rate measurements in reinforced concrete. Corros. Sci. 46 (2004) 2467-2485.

[34] C. Andrade. C. Alonso. On site measurements of corrosion rate of reinforcements. Constr. Build. Mater. 15 (2001) 141-145.

[35] E. Moreno, A. Cobo, G. Palomo, M.N. González. Mathematical models to predict the mechanical behaviour of reinforcements depending on their degree of corrosion and the diameter of the rebars. Constr. Build. Mater. 61 (2014) 156-163. https://doi.org/10.1016/j.conbuildmat.2014.03.003.

[36] A.M. Bazán, A. Cobo, J. Montero. Study of mechanical properties of corroded steels embedded in concrete with the modified surface length. Constr. Build. Mater. 117 (2016) 80-87. https://doi.org/10.1017/jconbuildmat.2016.04.109.

[37] G. Monrrabal, A. Bautista, S. Guzman, C. Gutierrez, F. Velasco. Influence of the cold working induced martensite on the electrochemical behavior of AISI 304 stainless steel surfaces. J. Mater. Res. Techn*. (in press).* https://doi.org/10.1016/j.jmrt.2018.10.004

[38] ASTM 876-15. Standard Test Method for Corrosion Potentials of Uncoated Reinforcing Steel in Concrete

[39] C Alonso, C Andrade, M Castellote, P Castro Chloride threshold values to depassivate reinforcing bars embedded in a standardized OPC mortar. Cem. Concrete Res.30 (2000) 1047-1055. https://doi.org/10.1016/S0008-8846(00)00265-9

[40] V.K. Gouda, Corrosion and corrosion inhibition of reinforcing steel. Br. Corros. J. 5 (1970) 198-203. https://doi.org/10.1179/000705970798324450

[41] S. Mundra, M. Criado, S.A. Bernal, J.L. Provis. Chloride-induced corrosion of steel rebars in simulated pore solutions of alkali-activated concretes. Cement Concrete Res. 100 (2017) 385-397. https://doi.org/10.1016/j.cemconres.2017.08.006

[42] A. Pachón-Montaño, J. Sánchez-Montero, C. Andrade, J. Fullea, E. Moreno, V. Matres. Threshold concentration of chlorides in concrete for stainless steel reinforcement: Classic austenitic and new duplex stainless steel. Constr. Build. Mater. 186 (2018) 495-502. https://doi.org/10.1016/j.conbuildmat.2018.07.081

[43] J. Shi, J. Ming, W. Sun, Y. Zhang. Corrosion performance of reinforcing steel in concrete under simultaneous flexural load and chlorides attack. Constr. Build. Mater. 149 (2017) 315-326. https://doi.org/10.1016/j.conbuildmat.2017.05.092

[44] D.V. Ribeiro, J.C.C. Abrantes. Application of electrochemical impedance spectroscopy (EIS) to monitor the corrosion of reinforced concrete: A new approach. Constr. Build. Mater. 111 (2016) 98-104. https://doi.org/10.1016/j.conbuildmat.2016.02.047

[45] A. Bautista, E.C. Paredes, S.M. Alvarez. F. Velasco. Welded, sand-blasted stainless steel corrugated bars in non-carbonated and carbonated mortars: A 9-year corrosion study. Corros. Sci. 102 (2016) 363-372. https://doi.org/10.1016/j.corsci.2015.10.029

Tables

Click here to download Table: TABLES.docx

TABLES

Table 1. Chemical composition of the studied B-500-SD bars.

Chemical composition (%)								
C	**Mn**	**S**	**Si**	**Cu**	**Ni**	**Mo**	**V**	**Fe**
0.21	0.86	0.02	0.29	0.34	0.09	0.02	<0.001	Balance

Table 2. Results obtained from the simulation of the EIS spectra obtained in simulated pore solution.

	R_{sol} ($\Omega \cdot cm^2$)	R_{pas} ($\Omega \cdot cm^2$)	C_{pas} ($\mu F \cdot cm^2 \cdot s^{n-1}$)	n_{pas}	R_{pit} ($k\Omega \cdot cm^2$)	C_{pit} ($\mu F \cdot cm^2 \cdot s^{n-1}$)	n_{dl}	Ws-R ($k\Omega \cdot cm^2$)	Ws-T (s)	Ws-P
Ribbed surface	7.1±0.5	13±5	78±24	0.81±0.03	**5**±2	151±56	0.77±0.01	**4**±1	85±7	0.50±0.01
Core	6.7±0.4	13±1	32±5	0.89±0.04	**13**±5	48±5	0.87±0.03	**7**±1	9±5	0.43±0.03
Galvanic couple	7.6±0.5	14±2	7±2	0.80±0.01	**11**±1	100±5	0.78±0.01	**7**±2	19±4	0.50±0.01

Table 3. Results of the reinforced concrete slabs summited to accelerated corrosion.

	Accelerated corrosion time	**Mass loss of the bars** (%)	**Corrosion rate of the bars** (mg cm^{-2} day^{-1})	**Number of cracks**	**Maximum crack width range** (mm)	**Supplied charge** ($kC \cdot cm^{-2}$)	**Current efficiency** (%)
Slab 1	**70 days**	5.6 ± 0.7	1.7 ± 0.2	3	0.2-0.6	4.8	88 - 132
Slab 2	**120 days**	8.2 ± 0.8	1.5 ± 0.1	5	0.3-1.1	8.2	74 - 111
Slab 3	**160 days**	9.5 ± 1.0	1.3 ± 0.1	3	1.0-1.4	9.8	73 - 109
Slab 4	**220 days**	10.7 ± 1.6	1.0 ± 0.2	4	1.7-3.0	12.3	65 - 97
Slab 5	**280 days**	10.9 ± 1.8	0.8 ± 0.2	6	0.6-5.0	9.8	84 - 126
Slab 6	**350 days**	11.4 ± 1.0	0.7 ± 0.1	7	2.0-6.0	11.4	76 - 114

Figure legends

Figure 1. Image of the samples used for the electrochemical studies in simulated pore solution.

Figure 2. Image of one of the reinforced slabs that has been submitted to accelerated corrosion

Figure 3. Cross sectional images of the TMT reinforcing bar: a) whole cross-sectional view; b) microstructure of the core of the bar; c) microstructure of the transition region; d) microstructure of the outer region of the bar.

Figure 4. Microhardness profiles carried out on cross sections of the bars.

Figure 5 Example of one of the registered time records corresponding to the i_{galv} flowing between samples of corrugated surface of the bars and samples form the core of the bars, when they are short-circuited and immersed in simulated pore solution.

Figure 6. Examples of polarization curves in simulated pore solution.

Figure 7. Results obtained from polarization curves as those shown in Figure 6: a) values corresponding to the i_{corr} and the E_{corr} of the studied samples; b) Tafel slopes calculated for the studied systems.

Figure 8. Examples of the EIS spectra obtained in simulated pore solution and plotted using a) Bode; and b) Nyquist diagrams.

Figure 9. Equivalent circuit used to simulate the obtained EIS spectra.

Figure 10. Macroscopic images of the bars corroded inside the concrete slabs after the acid etching cleaning: a) examples of the attack in some of the bars corroded for 220 days; b) big pits formed in the surface of one the bars corroded for 280 days.

Figure 11. Cross sectional views of pits generated in bars embedded in a chloride contaminated concrete slab. a) Pit with a moderate depth; b) Deep pit.

Figure 12. Example of the optoelectronic microcopy image for pit generated in a chloride contaminated concrete slab.

Figure 13. Relationship between the mass loss of each pit and its mouth surface. Results obtained from the optoelectronic characterization of the main pits formed on the six different studied chloride contaminated concrete slabs.

Figure 14. Relationship between the mass loss of each pit and its maximum depth. Results obtained from the optoelectronic characterization of the main pits formed on the six different studied chloride contaminated concrete slabs.

Figure 1
Click here to download Figure: Figure 1.docx

Figure 1

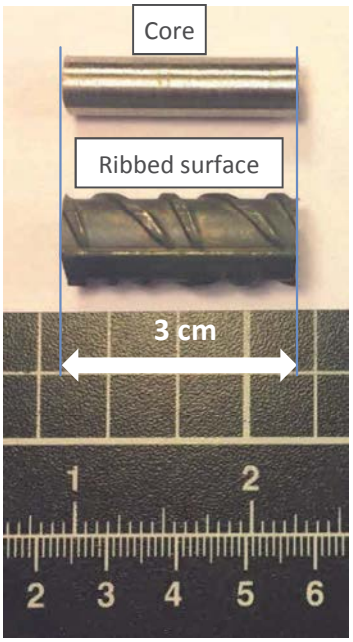

Figure 2
Click here to download Figure: Figure 2.docx

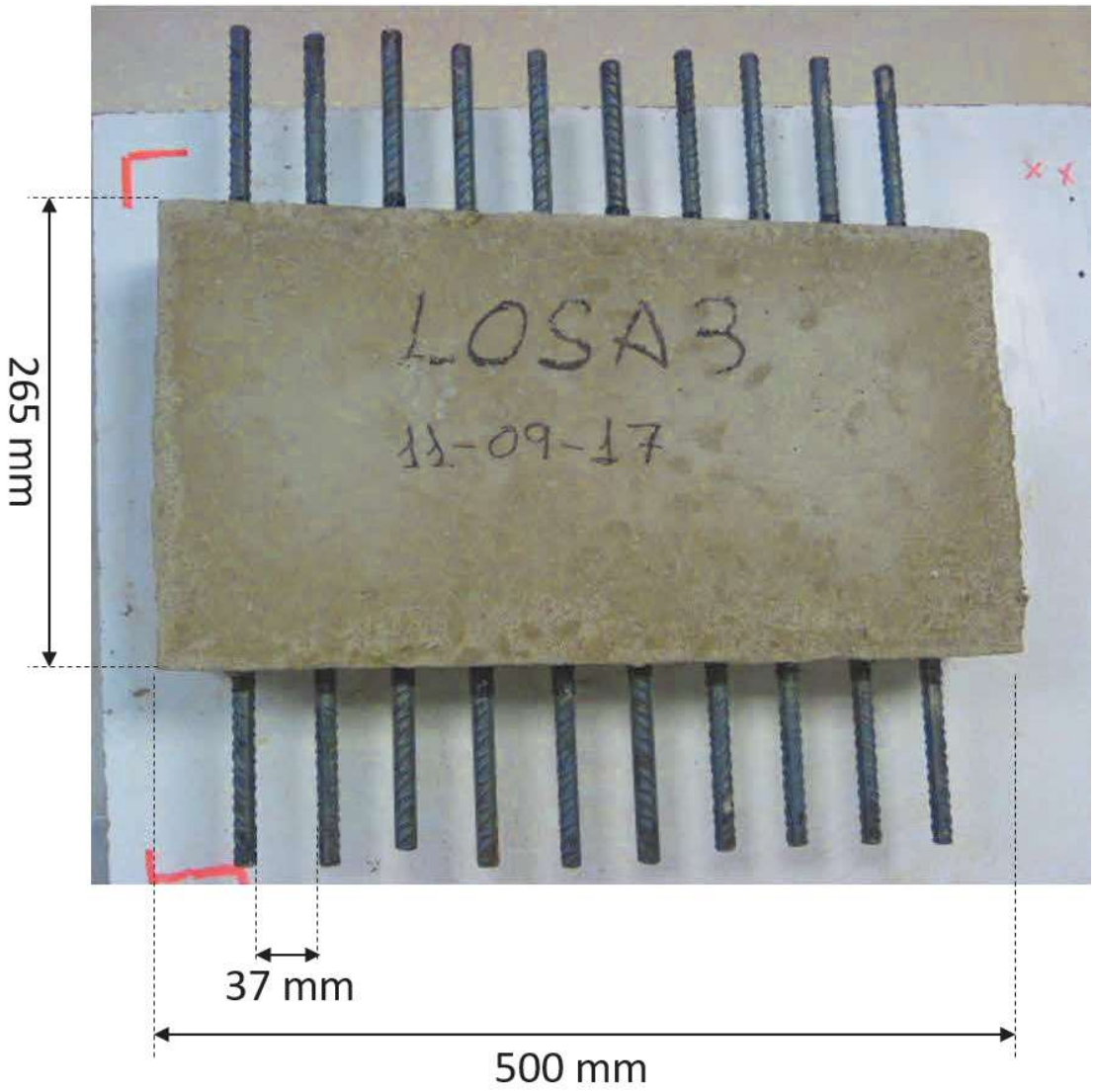

Figure 2

Figure 3
Click here to download Figure: Figure 3 new.docx

Figure 3

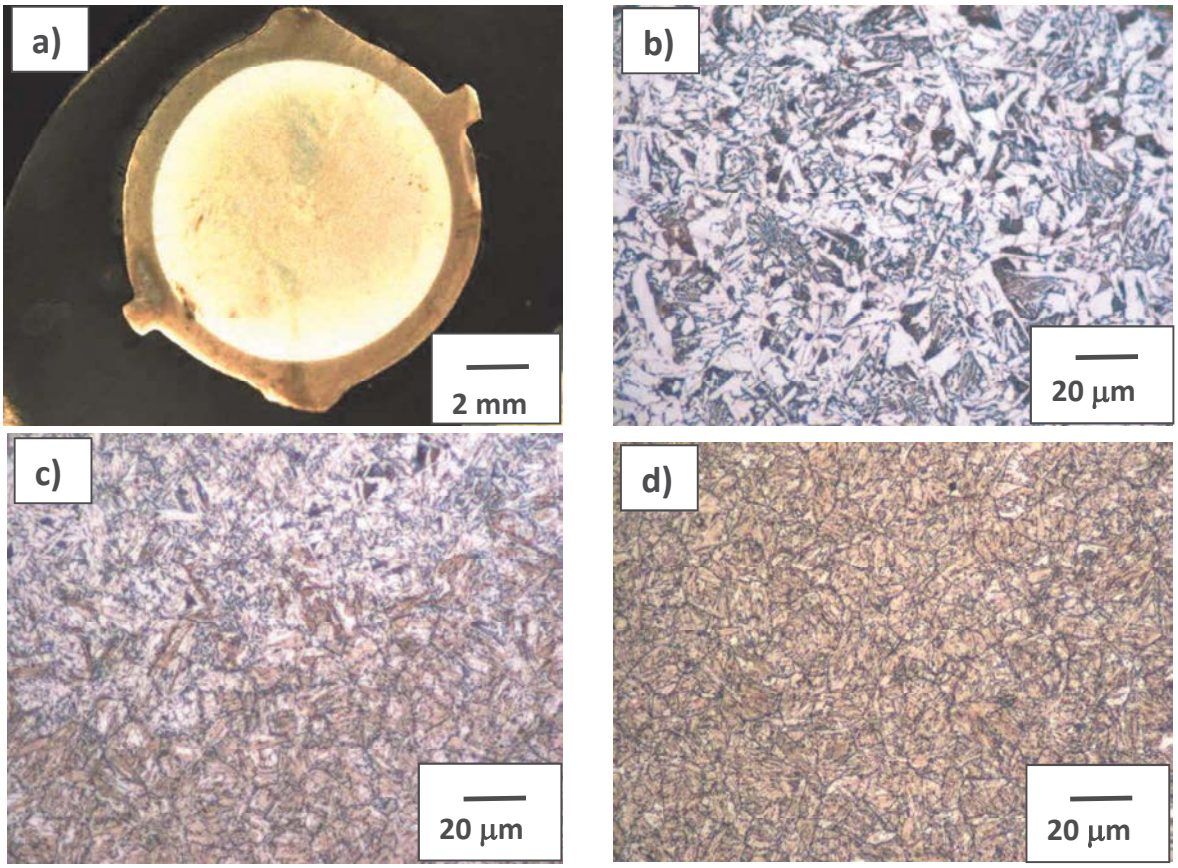

Figure 4
Click here to download Figure: Figure 4 new.docx

Figure 4

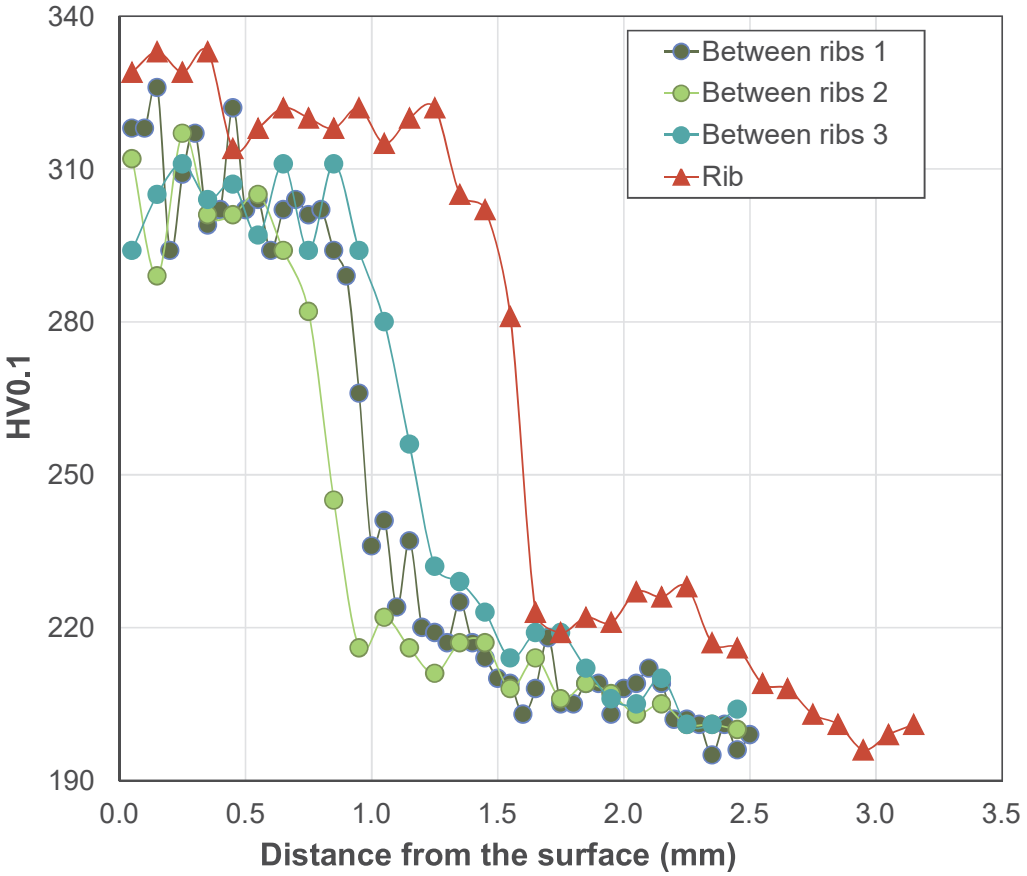

Figure 5
Click here to download Figure: Figure 5 new.docx

Figure 5

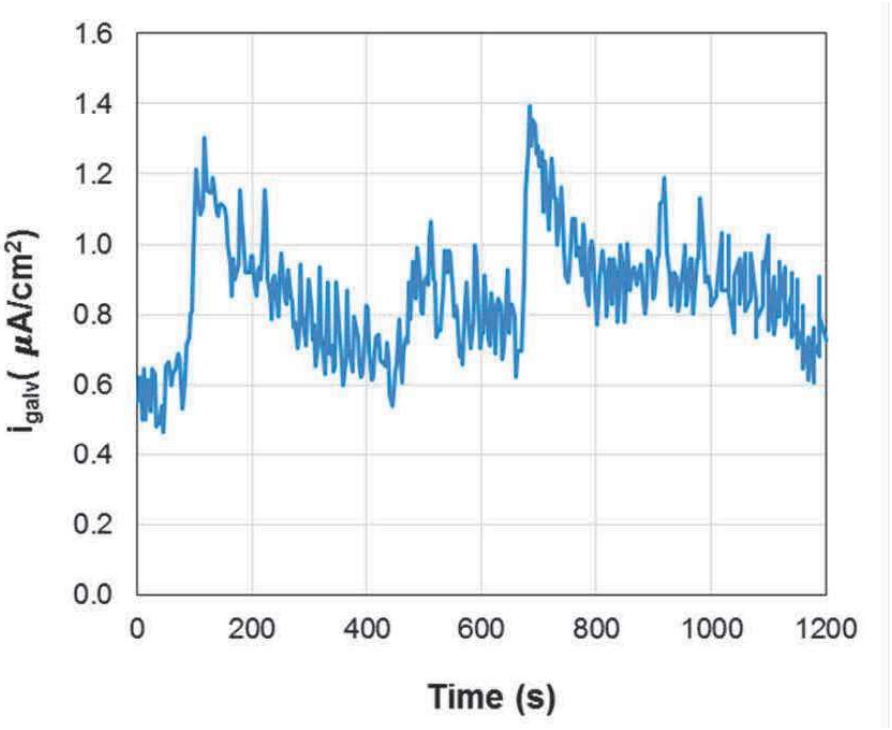

Figure 6
Click here to download Figure: Figure 6 new.docx

Figure 6

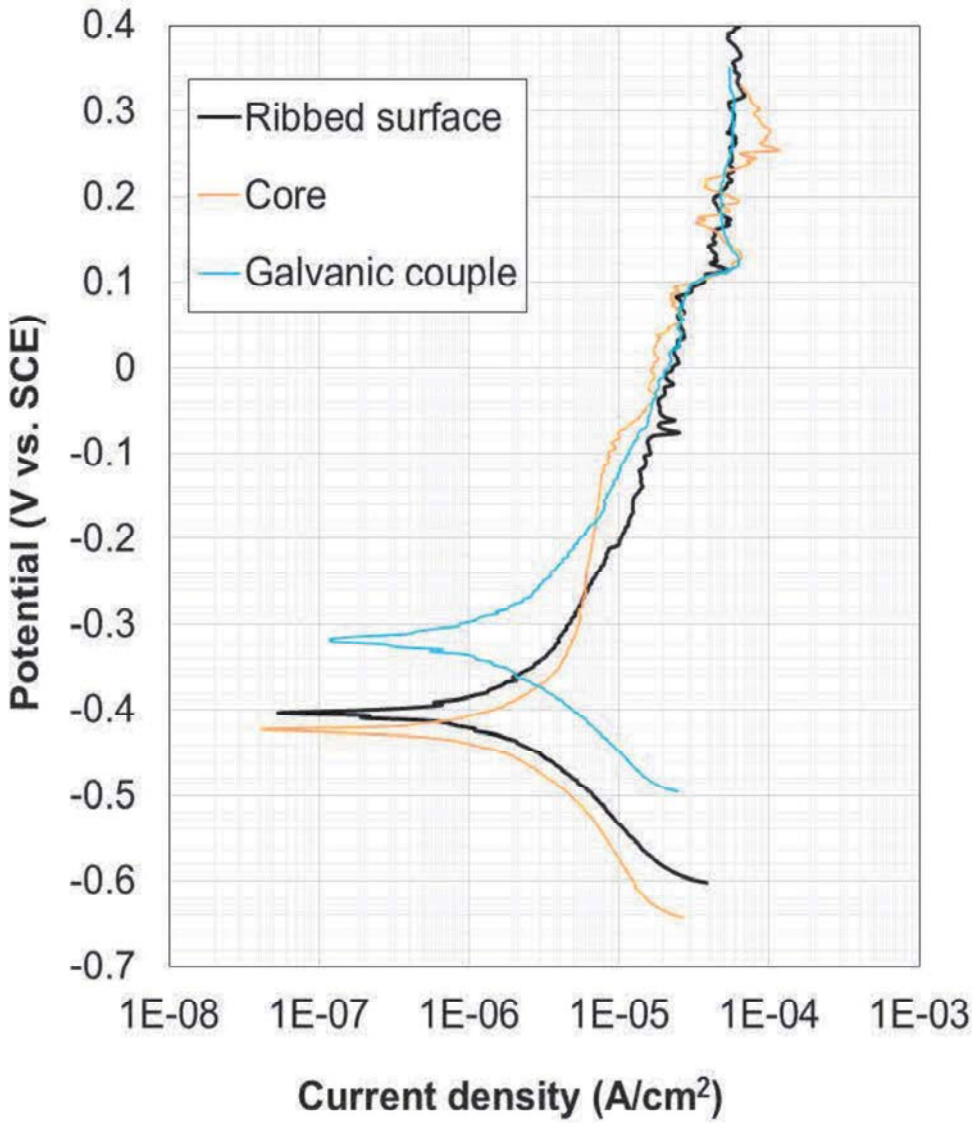

Figure 7
Click here to download Figure: Figure 7 new.docx

Figure 7

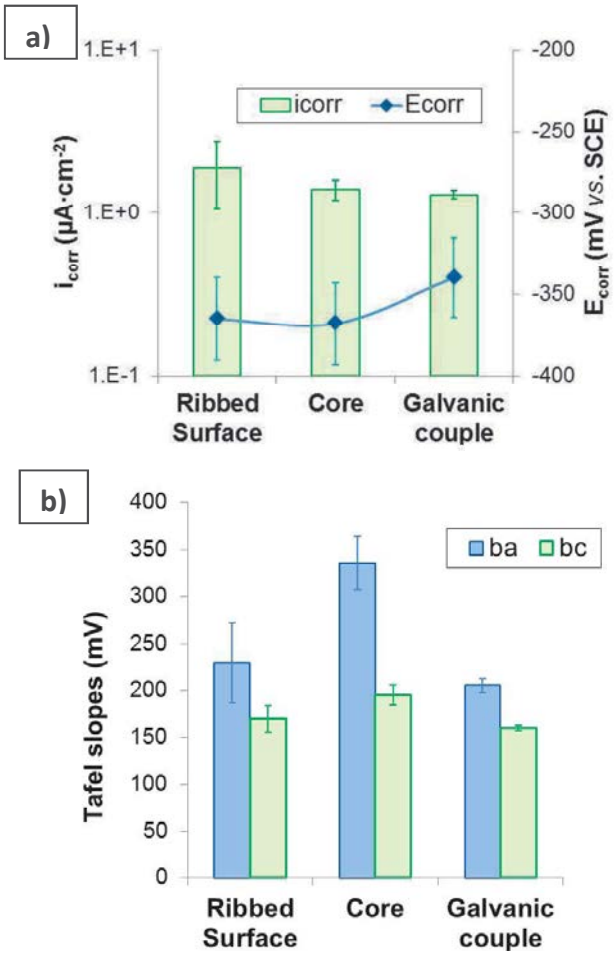

Figure 8

Click here to download Figure: Figure 8new.docx

Figure 8

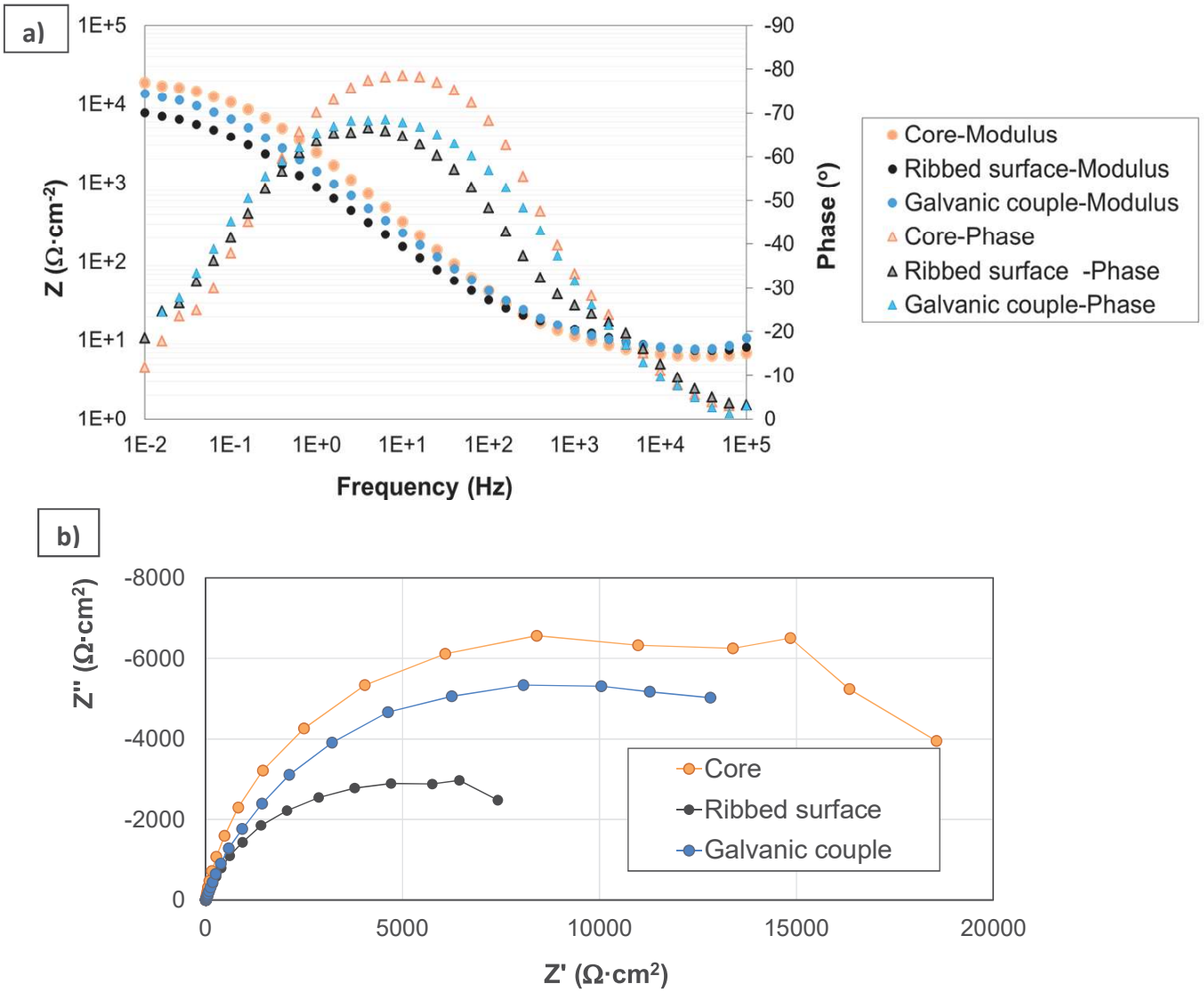

Figure 9
Click here to download Figure: Figure 9 new.docx

Figure 9

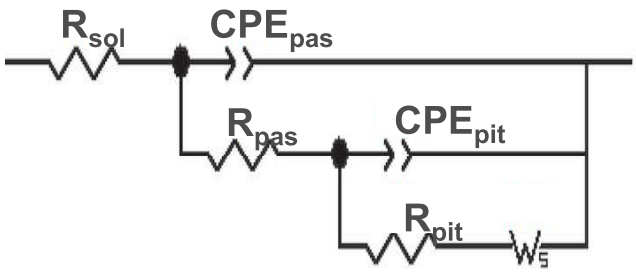

Figure 10
Click here to download Figure: Figure 10new.pdf

Figure 10

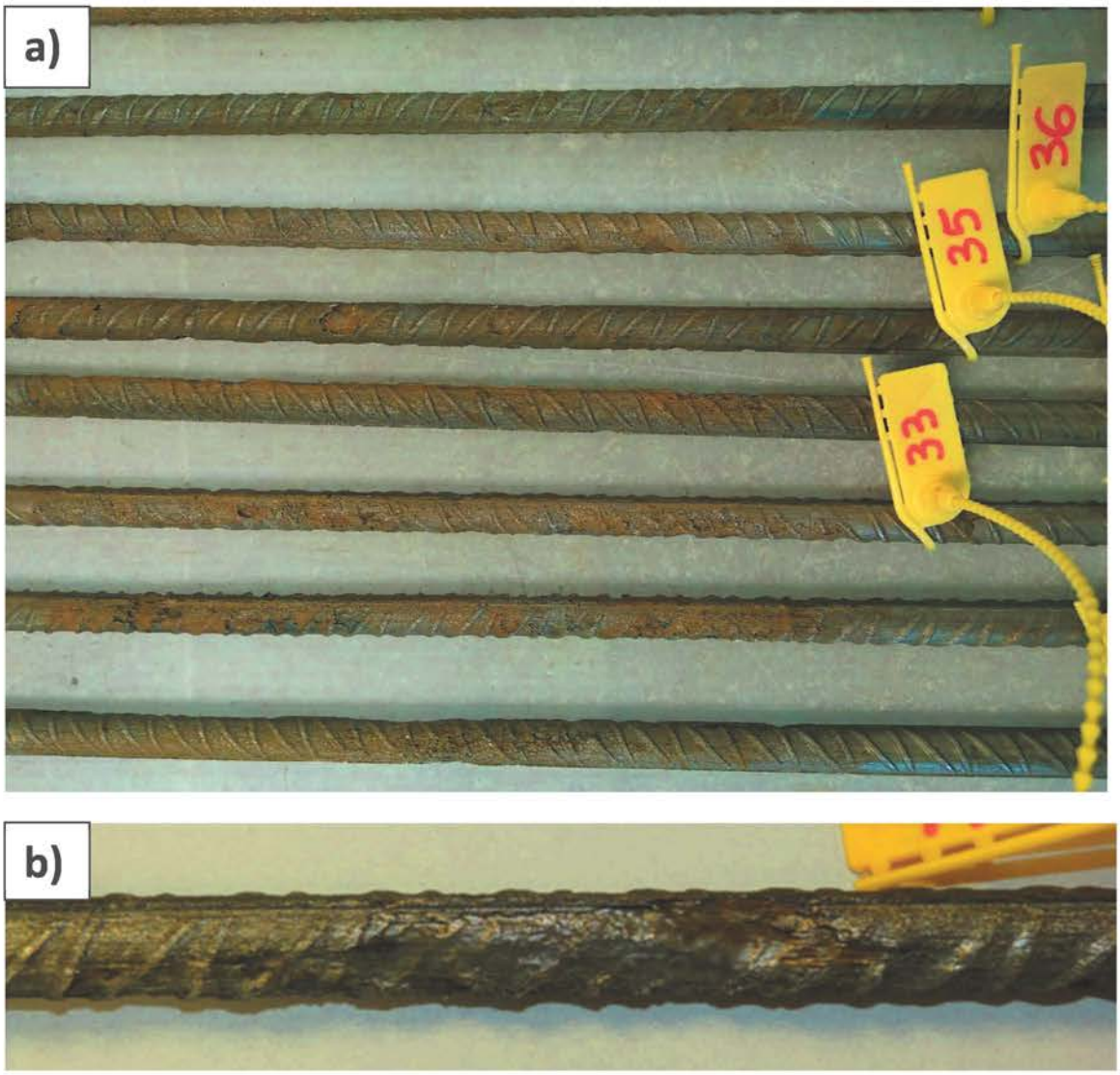

Figure 11
Click here to download Figure: Figure 11 new.docx

Figure 11

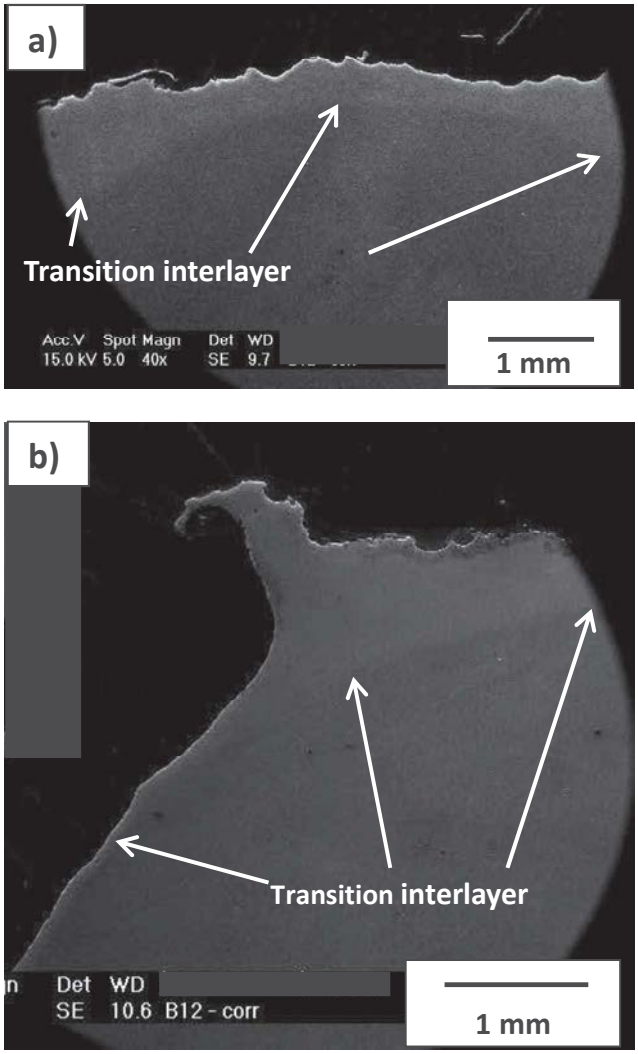

Figure 12
Click here to download Figure: Figure 12.docx

Figure 12

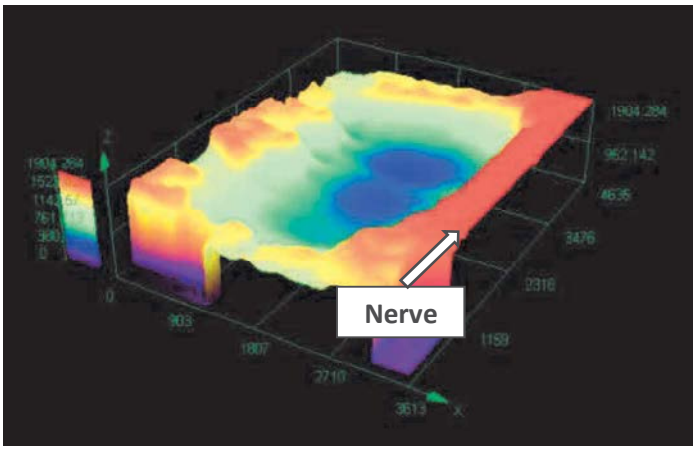

Figure 13
Click here to download Figure: Figure 13.docx

Figure 13

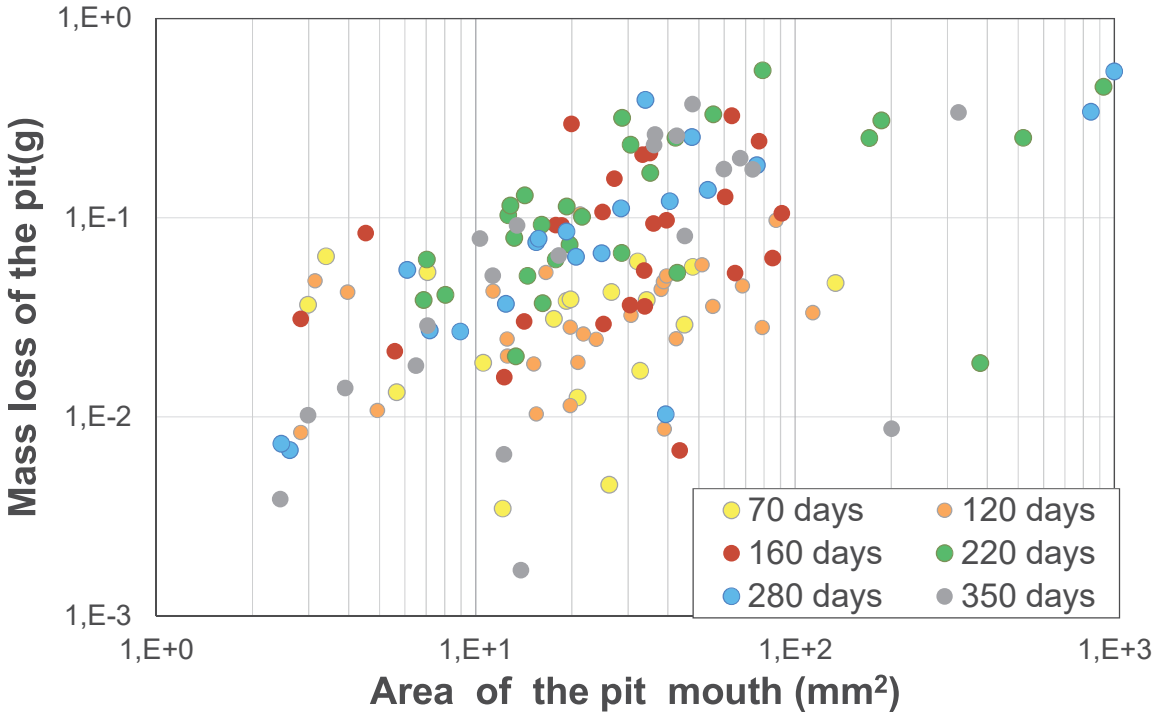

Figure 14
Click here to download Figure: Figure 14.docx

Figure 14